UNIVERSITY
OF TRENTO

DEPARTMENT OF INFORMATION AND COMMUNICATION TECHNOLOGY

38050 Povo – Trento (Italy), Via Sommarive 14
http://www.dit.unitn.it

FULL-VECTORIAL THREE-DIMENSIONAL MICROWAVE IMAGING THROUGH THE ITERATIVE MULTI-SCALING STRATEGY – A PRELIMINARY ASSESSMENT

G. Franceschini, D. Franceschini, and A.Massa

June 2005

Technical Report DIT-05-010

Full-Vectorial Three-Dimensional Microwave Imaging through the Iterative Multi-Scaling Strategy - A Preliminary Assessment

Gabriele Franceschini, Davide Franceschini, and Andrea Massa, *Member*, *IEEE*

Department of Information and Communication Technologies,

University of Trento, Via Sommarive 14, I-38050 Trento - Italy

Tel. +39 0461 882057, Fax +39 0461 882093

E-mail: *andrea.massa@ing.unitn.it*, {*gabriele.franceschini*, *davide.franceschini*}*@dit.unitn.it*

Web-page: *http://www.eledia.ing.unitn.it*

Full-Vectorial Three-Dimensional Microwave Imaging through the Iterative Multi-Scaling Strategy - A Preliminary Assessment

Gabriele Franceschini, Davide Franceschini, and Andrea Massa

Abstract

In this paper, a multi-scaling strategy for full-vectorial three-dimensional inverse scattering problems is presented. The approach is fully iterative and it avoids solving any forward problem at each step. Thanks to the adaptive multi-resolution model, which offers considerable flexibility for the inclusion of the *a-priori* knowledge and of the knowledge acquired during the iterative steps of the multi-scaling process, the overall computational burden as well as the dimension of the search-space is considerably reduced. This allows to balance effectively the trade-off between computational costs and achievable resolution accuracy. The effectiveness of the proposed approach is demonstrated through a selected set of preliminary experiments using homogeneous dielectric scatterers in a noisy synthetic environment.

Key words:

Three-Dimensional Geometry, Microwave Imaging, Inverse Scattering, Iterative Multi-Scaling Method.

1 Introduction

In the framework of microwave imaging, large efforts have been devoted in the last years to develop reliable inverse scattering techniques (for an overview, see [1] and the references cited therein). However, several contributions are concerned with tomographic configurations and a limited literature is available for three-dimensional (3D) imaging due to its computational complexity.

The use of the two-dimensional (2D) approximation simplifies the computations since in such a case the problem is generally reduced from vectorial to scalar and the dimension of the solution-space significantly reduces. Despite the approximation, the 2D hypothesis is appropriate in many cases and in several working conditions. However, a general treatment is not amenable to a 2D formalism and a full-vectorial 3D formulation is needed, although there are good examples of good 2D imaging algorithms which have proven to be useful in practice, including phantom and even clinical imaging experiments.

It is well known that the main limitation of 3D imaging is the intractable nature of the problem when a high spatial resolution is required. On the other hand, several applications ranging from biomedical diagnostics to subsurface sensing generally require detailed reconstructions. In order to faithfully solve such a problem allowing a good trade-off between reconstruction accuracy and computational burden, some attempts have been carried out.

In [2] and [3], Born and Rayleigh approximations are used to develop linearized space-domain inversion methods able to effectively deal with three-dimensional weak scatterers. Moreover, concerning imaging of dielectric targets embedded in a lossy half-space at radar frequencies, a modified form of the extended Born forward model in concert with the iterative Born method is analyzed in [4].

As far as nonlinear approaches are concerned, Harada *et al.* [5] extended a 2D gradient-based optimization method to three-dimensional configurations by assuming an *a-priori* knowledge on outer boundaries of the scatterers to facilitate the retrieval process.

On the other hand, an extension of the contrast source inversion (CSI) method for handling the full-vector complex 3D cross-well induction logging problem is considered in [6]. In that paper, the cost functional of the CSI method has been modified including a preconditioning operator obtained by using the concept of the extended Born approximation, which accelerates the convergence and allows the reconstruction of large contrasts.

In order to model strong 3D multiple scattering effects in biomedical imaging applications, Zhang and Liu [7] developed a nonlinear inverse scattering approach based on an improved version of the CSI method. To accelerate the reconstruction process, the fast Fourier transform algorithm is adopted.

In this paper, a different methodological approach is proposed by extending the iterative multi-scaling approach (IMSA) for the 2D case [8]. Neither approximations nor acceleration techniques are used. The original problem is iteratively solved by considering a succession of reconstructions aimed at defining a finer spatial resolution in a limited region of the investigation domain. The result turns out to be a reliable numerical inversion procedure able to limit the computational burden as well as the computer memory requirements.

The paper is organized as follows. In Section 2, the mathematical model and the geometry of the 3D full-vectorial inverse scattering problem are described. A suitable full-vectorial three-dimensional strategy based on an iterative multi-resolution process is then presented in Section 3. The results of a selected set of numerical experiments are shown in Section 4 to validate the proposed strategy pointing out potentialities and current limitations. Conclusions follow (Sect. 5).

2 Problem Formulation

Let us consider a dielectric scatterer characterized by an object function $\tau(\underline{r}) = [\varepsilon_r(\underline{r}) - 1] - j\frac{\sigma(\underline{r})}{2\pi f \varepsilon_0}$ ($\varepsilon_r(\underline{r})$ and $\sigma(\underline{r})$ being the relative dielectric permittivity and the electric conductivity, respectively) and contained inside a space region called investigation domain D_{ind}

(Fig. 1). Such a region is illuminated by a monochromatic (f being the working frequency) incident electromagnetic wave whose space-dependent part is characterized by a known electric field vector $\underline{E}_v^{inc}(\underline{r})$, v being the view index since a multi-illumination system is used [9]. For each illumination ($v = 1, ..., V$), the scattered field $\underline{E}_v^{scatt}(\underline{r}_{m_{(v)}})$ is collected at discrete observation points $\underline{r}_{m_{(v)}} \in D_{oss}$, $m_{(v)} = 1, ..., M^{(v)}$ (D_{oss} being the observation domain external to the investigation domain, $D_{oss} \notin D_{ind}$).

According to [10] and omitting the time-dependence factor $e^{j2\pi ft}$, the arising scattering phenomena are mathematically described through the following integral equations:

$$\underline{E}_v^{scatt}(\underline{r}_{m_{(v)}}) = \int_{D_{ind}} \tau(\underline{r}')\underline{E}_v(\underline{r}') \cdot \underline{\underline{G}}\left(\underline{r}_{m_{(v)}} \middle| \underline{r}'\right) d\underline{r}' \quad \underline{r}_{m_{(v)}} \in D_{oss} \quad m_{(v)} = 1, ..., M^{(v)} \tag{1}$$

$$\underline{E}_v^{inc}(\underline{r}) = \underline{E}_v(\underline{r}) - \int_{D_{ind}} \tau(\underline{r}')\underline{E}_v(\underline{r}') \cdot \underline{\underline{G}}(\underline{r}|\,\underline{r}')\, d\underline{r}' \quad \underline{r} \in D_{ind} \quad v = 1, ..., V \tag{2}$$

where $\underline{\underline{G}}(\underline{r}|\,\underline{r}')$ is the dyadic Green's function for free space given by

$$\underline{\underline{G}}(\underline{r}|\,\underline{r}') = \frac{1}{4\pi}\left[\underline{\underline{I}} + \frac{1}{k^2}\nabla\nabla\right] \frac{exp(-jk|\underline{r}-\underline{r}'|)}{|\underline{r}-\underline{r}'|} \tag{3}$$

k being the free-space wavenumber. To numerically manage the inverse problem, Eqs. (1)-(2) are discretized according to the moment method [11]

$$E_{v,i}^{scatt}(\underline{r}_{m_{(v)}}) = \sum_{n=1}^{N}\left\{\sum_{h=x,y,z}\left[\tau\left(\underline{r}_n\right) E_{v,h}\left(\underline{r}_n\right) G_{hi}\left(\underline{r}_{m_{(v)}} \middle| \underline{r}_n\right)\right]\right\} \quad \underline{r}_{m_{(v)}} \in D_{oss} \quad i = x, y, z \tag{4}$$

$$E_{v,i}^{inc}(\underline{r}_n) = E_{v,i}(\underline{r}_n) - \sum_{q=1}^{N}\left\{\sum_{h=x,y,z}\left[\tau\left(\underline{r}_q\right) E_{v,h}\left(\underline{r}_q\right) G_{hi}\left(\underline{r}_n|\,\underline{r}_q\right)\right]\right\} \quad \underline{r}_n \in D_{ind} \tag{5}$$

where N indicates the number of discretization subdomains of D_{ind} and $G_{hi}\left(\underline{r}_n|\,\underline{r}_q\right)$ is computed as in [12].

Because of the ill-conditioning of the arising algebraic system (4)-(5), a minimum least-square solution is looked for by defining a suitable cost function to be minimized by means of an optimization technique. However, in forming a detailed image of the scenario under test, the main drawback of such a "bare" approach (already pointed out in two-

dimensional applications, but certainly sharpened when three-dimensional configurations are dealt with) is the arising computational complexity in terms of dimension of the solution space [proportional to $U = (3V + 1) \times N$] as well as the convergence rate (which strictly depends on U) making the 3D inversion intractable.

As highlighted in the reference literature concerned with two-dimensional inversion problems [13][14][15][8][16], an adequate trade-off between computational burden and spatial resolution accuracy can be obtained by resorting to suitable multi-resolution strategies. In the following, an extension of the multi-scaling multi-resolution approach [8] will be proposed for the full-vectorial three-dimensional case in hand.

3 Reconstruction Strategy

It is well known that multi-resolution representations are very effective for describing the information content of an image or of a complex scenario, since the structures to be recognized have different sizes. Moreover, it is not possible or too expensive from a computational point-of-view to define *a-priori* an optimal resolution for such an analysis. Therefore, especially in a three-dimensional framework, it could be profitable to process inverse scattering data by reorganizing the unknown image into a set of details appearing at different resolutions to be determined according to an iterative multi-scaling strategy. As a matter of fact, such a progressive coarse-to-fine representation of the scenario provides a simple hierarchical method for interpreting the reconstructed-profile formation. In general, different resolutions characterize different physical structures of the scenario under test. At a coarse resolution, the details of the image describe larger structures (e.g., the homogeneous background), which provide the so-called "image context". Thus, it is quite natural to firstly analyze the details at a coarse resolution and then gradually to increase the resolution taking into account the information on the scenario under test previously gained and corresponding to a rough representation.

Mathematically, such an iterative multi-scaling analysis of the investigation domain

can be implemented by defining, at each step s, a three-dimensional multi-resolution cost function to be minimized and by determining the so-called *Region-of-Interest* (RoI), $D_{(s)}$, (i.e., the region of D_{ind} where the scatter is supposed to be located) according to its descriptors. More in detail, the cost function assumes the following form

$$\Phi^{(s)}\left\{\tau\left(\underline{r}_{n_{(r)}}\right),\, E_{v,i}\left(\underline{r}_{n_{(r)}}\right)\right\} = \sum_{v=1}^{V}\sum_{m=1}^{M}\sum_{i=x,y,z}\Phi^{Data}_{v,m,i}\left\{\tau\left(\underline{r}_{n_{(r)}}\right),\, E_{v,i}\left(\underline{r}_{n_{(r)}}\right)\right\}$$
$$+\sum_{v=1}^{V}\sum_{r=1}^{R}\sum_{n_{(r)}=1}^{N_{(r)}}\sum_{i=x,y,z}\Phi^{State}_{v,n_{(r)},i}\left\{\tau\left(\underline{r}_{n_{(r)}}\right),\, E_{v,i}\left(\underline{r}_{n_{(r)}}\right)\right\} \quad r=1,...,R=s;\quad n_{(r)}=1,...,N_{(r)} \tag{6}$$

$$\Phi^{Data}_{v,m,i}\left\{\tau\left(\underline{r}_{n_{(r)}}\right),\, E_{v,i}\left(\underline{r}_{n_{(r)}}\right)\right\} = \frac{1}{\left|E^{scatt}_{v,i}(\underline{r}_{m_{(v)}})\right|^2}$$
$$\left|E^{scatt}_{v,i}(\underline{r}_{m_{(v)}}) - \sum_{h=x,y,z}\left\{\sum_{r=1}^{R}\sum_{n_{(r)}=1}^{N_{(r)}}\left[w\left(\underline{r}_{n_{(r)}}\right)\tau\left(\underline{r}_{n_{(r)}}\right)E_{v,h}\left(\underline{r}_{n_{(r)}}\right)G_{hi}\left(\underline{r}_{m_{(v)}}\middle|\,\underline{r}_{n_{(r)}}\right)\right]\right\}\right|^2 \tag{7}$$

$$\Phi^{State}_{v,n_{(r)},i}\left\{\tau\left(\underline{r}_{n_{(r)}}\right),\, E_{v,i}\left(\underline{r}_{n_{(r)}}\right)\right\} = \frac{w\left(\underline{r}_{n_{(r)}}\right)}{\left|E^{inc}_{v,i}\left(\underline{r}_{n_{(r)}}\right)\right|^2}$$
$$\left|E^{inc}_{v,i}\left(\underline{r}_{n_{(r)}}\right) - E_{v,i}\left(\underline{r}_{n_{(r)}}\right) + \sum_{h=x,y,z}\sum_{z=1}^{R}\sum_{q_{(z)}=1}^{N_{(z)}}\left\{\tau\left(\underline{r}_{q_{(z)}}\right)E_{v,h}\left(\underline{r}_{q_{(z)}}\right)G_{hi}\left(\underline{r}_{q_{(z)}}\middle|\,\underline{r}_{q_{(z)}}\right)\right\}\right|^2 \tag{8}$$

where

$$w\left(\underline{r}_{n_{(r)}}\right) = \begin{cases} 0 & if \quad \underline{r}_{n_{(r)}} \notin D_{(s-1)} \\ 1 & if \quad \underline{r}_{n_{(r)}} \in D_{(s-1)} \end{cases} \tag{9}$$

R being the finest resolution level at the s-th step ($R=s$) and $N_{(r)}$ the number of cubic sub-domains related to the r-th resolution level.

Moreover, the RoI's descriptors are its center whose coordinates are computed as follows

$$x_C^{(s-1)} = \frac{\sum_{r=1}^{R}\sum_{n_{(r)}=1}^{N_{(r)}}\left\{x_{n_{(r)}}\tau\left(\underline{r}_{n_{(r)}}\right)\right\}}{\sum_{n_{(r)}=1}^{N_{(r)}}\left\{\tau\left(\underline{r}_{n_{(r)}}\right)\right\}};\quad y_C^{(s-1)} = \frac{\sum_{r=1}^{R}\sum_{n_{(r)}=1}^{N_{(r)}}\left\{y_{n_{(r)}}\tau\left(\underline{r}_{n_{(r)}}\right)\right\}}{\sum_{n_{(r)}=1}^{N_{(r)}}\left\{\tau\left(\underline{r}_{n_{(r)}}\right)\right\}}$$
$$z_C^{(s-1)} = \frac{\sum_{r=1}^{R}\sum_{n_{(r)}=1}^{N_{(r)}}\left\{z_{n_{(r)}}\tau\left(\underline{r}_{n_{(r)}}\right)\right\}}{\sum_{n_{(r)}=1}^{N_{(r)}}\left\{\tau\left(\underline{r}_{n_{(r)}}\right)\right\}} \quad R=s-1 \tag{10}$$

and the RoI's side

$$L_C^{(s-1)} = 2\frac{\sum_{r=1}^{R}\sum_{n_{(r)}=1}^{N_{(r)}}\left\{\frac{\rho_{n_{(r)}}c_{(s-1)}\tau\left(\underline{r}_{n_{(r)}}\right)}{max_{n_{(r)}=1,..,N_{(r)}}\left\{\tau\left(\underline{r}_{n_{(r)}}\right)\right\}}\right\}}{\sum_{r=1}^{R}\sum_{n_{(r)}=1}^{N_{(r)}}\left\{\frac{\tau\left(\underline{r}_{n_{(r)}}\right)}{max_{n_{(r)}=1,..,N_{(r)}}\left\{\tau\left(\underline{r}_{n_{(r)}}\right)\right\}}\right\}}. \tag{11}$$

The multi-scaling process is iterated ($s \rightarrow s+1$) until a "*stationariness*" condition holds ($s = S_{opt}$)

$$\eta_u^{(s)} = \left\{\frac{\left|u_c^{(s+1)} - u_c^{(s)}\right|}{\left|u_c^{(s+1)}\right|} \times 100\right\} < \eta_u \quad u = x,\, y,\, z,\, L \tag{12}$$

where η_u, $u = x,\, ,y,\, z,\, L$ are fixed thresholds.

4 Numerical Assessment

In this section, the results of a selected set of numerical simulations will be shown mainly to explore the feasibility of the iterative three-dimensional multi-scaling strategy and to preliminarily assess its effectiveness in reconstructing dielectric scatterers.

As regards to the numerical experiments, let us refer to the schematic view of the three-dimensional multi-illumination/multi-view measurement setup in Fig. 1. The investigation domain $L_{ind} = 1.2\,\lambda$-sided has been successively ($v = 1, ..., V,\, V = 4$) illuminated by means of a plane wave impinging from the direction $\theta_v^{inc} = \frac{\pi}{2}$ and $\varphi_v^{inc} = (v-1)\frac{\pi}{2}$. In such a configuration, the incident electric field vector is inclined of $\frac{\pi}{4}$ clockwise with respect to the z-axis. The point like receivers ($M_{(v)} = 21$), which operate simultaneously and measure three vector components, have been located in $G = 3$ rings at the positions $\rho_{m_{(v)}} = 2.93\,\lambda$, $\varphi_{m_{(v)}}^{scatt} = \varphi_v^{inc} + 2\pi(m_{(v)} - 1)\frac{G}{M_{(v)}}$, and $z_{v,m} = \left(1 - \left\lfloor\frac{m_{(v)}-1}{M_{(v)}}G\right\rfloor\right) z_0$ [1] ($z_0 = 0.06\,\lambda$) $m_{(v)} = 1, ..., M_{(v)}$ [17]. As far as the inverse scattering data are concerned (i.e., $\underline{E}_v^{scatt}(\underline{r}_{m_{(v)}})$ and $\underline{E}_v^{inc}(\underline{r})$), they have been generated by solving the direct problem through the method of moments with an uniform discretization of the investigation domain, $N = 25 \times 25 \times 25$. To simulate a real environment, such data have been corrupted

[1] Please note that $\lfloor\,\rfloor$ indicates the integer part of the argument.

by adding a gaussian noise with a fixed signal-to-noise ratio, SNR.

Concerning the IMSA, the RoI has been discretized into $N_{(R)} = 5 \times 5 \times 5$ subdomains and, in such a preliminary implementation, a deterministic minimization procedure has been adopted [18] ($K_s = 2000$, $s = 1, ..., S_{opt}$, K_s being the maximum number of iterations for the minimization). Even though a deterministic optimizer strongly depends on the initialization and suffers from the local minima problem, the use of an iterative multi-scaling approach reduces such a drawback imposing a convenient ratio between data and problem unknowns [19]. Certainly, the local minima problem would be completely eliminated by integrating the IMSA together a stochastic minimization technique. In such a framework, more recent optimization approaches to standard 2D inverse scattering problems developed at the *ELEDIALab* have been described elsewhere [20] and their integration into the full-vectorial 3D-IMSA will be a key-issue of future researches. Moreover, the stationariness thresholds have been heuristically fixed to the following values: $\eta_u = 2\,\%$, $u = x$, y, z and $\eta_L = 5\,\%$. The initial guess for the unknowns is that of the free-space ($\tau(\underline{r}) = 0.0$ and $\underline{E}_v(\underline{r}) = \underline{E}_v^{inc}(\underline{r})$, $\underline{r} \in D_{ind}$).

The first test case deals with a centered dielectric scatterer with an object function $\tau = 3.0$ whose volume is $0.3\,\lambda \times 0.3\,\lambda \times 0.3\,\lambda$. As an example, let us consider the reconstruction at the final step ($s = S_{opt} = 3$) when a noise characterized by a $SNR = 30\,dB$ has been superimposed to the data. As can be observed in Fig. 2, where two orthogonal volume slices of the reconstructed profile are shown, the proposed approach is able to correctly locate the scatterer as well as to estimate its dimensions as confirmed by the values the error figures at the convergence ($\rho^{(S_{opt})} = 8.41 \times 10^{-6}$ and $\Delta^{(S_{opt})} = 3.83 \times 10^{-2}$). These values are reported in Tab. I and they have been computed as follows

$$\rho = \frac{\sqrt{\left[x_C - x_C^{(S_{opt})}\right]^2 + \left[y_C - y_C^{(S_{opt})}\right]^2 + \left[z_C - x_C^{(S_{opt})}\right]^2}}{\lambda} \tag{13}$$

$$\Delta = \left| \frac{L_C - L_C^{(S_{opt})}}{L_C} \right|. \tag{14}$$

Furthermore, in order to give an idea of the quantitative imaging, also the following error figures have been computed

$$\gamma_{(j)} = \sum_{r=1}^{R} \frac{1}{N_{(r)}^{(j)}} \sum_{n_{(r)}=1}^{N_{(r)}^{(j)}} \left\{ \frac{\tau^{(S_{opt})}(\underline{r}_{n_{(r)}}) - \tau(\underline{r}_{n_{(r)}})}{\tau(\underline{r}_{n_{(r)}})} \right\} \times 100 \qquad (15)$$

where $j \Rightarrow tot$ when $(x, y) \in D_{ind}$, $j \Rightarrow int$ when the considered region lies inside the actual volume of the scatterer, and $j \Rightarrow ext$ otherwise. As can be noticed, the 3D-IMSA demonstrates good capabilities in avoiding artifacts as pointed out by the value of the external quantitative error, $\gamma_{ext}^{(S_{opt})} = 0.26$. On the other hand, the reconstruction of the scatterer-domain is not so accurate ($\gamma_{int}^{(S_{opt})} = 21.09$) since the resolution in the vertical direction is worse than those in the transversal plane. This is due to the limited number of illuminations and of receivers in the vertical direction.

The second experiments is aimed at assessing the robustness of the 3D-IMSA on the level of noise. Towards this end, the SNR has been varied from $30\,dB$ up to $10\,dB$ and the reconstruction process has been repeated twenty times for a fixed data combination to take into account the statistical nature of the noise generation.

As expected, when the noise level grows the minimization of (6) turns out to be more difficult and more steps are needed to achieve the convergence or the stationariness condition on the retrieved profile (Fig. 3)[(2)]. Probably, such limitations are due to the capabilities of the gradient-based minimization technique in sampling the solution space. Therefore, more efficient stochastic minimization tools should be used in order to increase the performance in heavy noisy conditions. The difficulties of the deterministic method in the cost function minimization cause a deterioration of the reconstruction accuracy as pointed out from the behaviors of the error figures shown in Fig. 4. More in detail, the localization error ρ increases of about 4 order in magnitude [Fig. $4(a)$] because of the presence of a retrieval noise diffused over the external background ($\gamma_{ext}\rfloor_{SNR=10\,dB} \cong 4.0$ vs. $\gamma_{ext}\rfloor_{SNR=30\,dB} = 0.26$).

[(2)]The spikes in the cost function occur when the investigation area is scaled and the supports of the basis functions are redefined. In such points, the minimization of the functional starts with an higher level of resolution.

To further assess the potentialities and current limitations of the 3D-IMSA, the second example deals with an off-centered location ($x_C = y_C = z_C = 0.15\,\lambda$) of the same scatterer of the previous example. For comparison purposes, the plots of the error figures concerned with such a geometry are reported in Fig. 4 together with those of the centered configuration.

The behaviors of the error figures clearly show that the reconstructions are worse in terms of ρ [Fig. $4(a)$] and γ_{int} [Fig. $4(c)$], while similar performance are yielded for the other error indexes [Figs. $4(b)$-(c)].

As an example, to have more details on the localization process, Fig. 5 shows the evolution of the contour plot during the multi-step procedure ($SNR = 30\,dB$). As can be observed, starting from an incorrect shaping of the scatterer ($s = 1$), the 3D-IMSA is able to refine the estimation of the scatterer perimeter and, at the end of the multi-step process ($s = S_{opt} = 3$), the contour of the object is faithfully determined.

Concerning the assessment of the proposed approach when dimensions of the unknown object become comparable to the wavelength of the incident wave, another experiment has been carried out varying the side of the off-centered object from $0.15\,\lambda$ up to $1.0\,\lambda$ ($SNR = 20\,dB$). The results of such an analysis are reported in Fig. 6 in terms of qualitative [Fig. $6(a)$] as well as quantitative [Fig. $6(b)$] error figures. Whatever the scatterer dimension, the capabilities both in locating and dimensioning the object are keep almost unaltered ($\rho < 1.5 \times 10^{-1}$ and $1.0 \times 10^{-1} < \Delta < 4.0 \times 10^{-1}$). On the contrary, the quantitative imaging gets worse. The total and external error figures (γ_{tot} and γ_{ext}) increase for larger scatterers, even though the reconstruction error concerned with the scatterer domain ($\gamma_{int} \cong 30$) is constant.

As far as the reconstruction of the scatterer-domain is concerned, the same behavior of the previous example verifies when the object function is varied in the range $\tau \in [1.0, 5.0]$ (Fig. 7). As for the centered object, the accuracy index of the quantitative scatterer-domain retrieval, γ_{int}, is not negligible and greater than the other errors [Fig. $7(b)$], Consequently, the quantitative imaging is not that accurate in all the cases, but once

again γ_{int} turns out to be almost insensitive to the object function value in the range $\tau \in [2.0, 5.0]$.

In order to verify whether an increasing of the number of illuminations improves the situation, different illumination configurations have been considered. For this purpose, various geometries of the imaging system have been taken into account. Firstly, the number of views of the cylindrical system has been increased from $V = 4$ up to $V = 8$. Successively, a spherical geometry has been used where $\theta_v^{inc} = \left\lfloor \frac{2v}{V} \right\rfloor \frac{\pi}{3}$, $\varphi_v^{inc} = \pi \frac{v}{V}$, $v = 0, ..., V-1$. In such a case, the $M_{(v)} = 21$ measurement points have been located at the angular coordinates $\theta_{m_{(v)}}^{scatt} = \theta_v^{inc} + m_{(v)} \frac{\pi}{M_{(v)}-1}$, $\varphi_{m_{(v)}}^{scatt} = \varphi_v^{inc} + m_{(v)} \frac{2G\pi}{M_{(v)}-1}$, $m_{(v)} = 0, ..., M_{(v)} - 1$, on a sphere $r = 2.93\,\lambda$ in radius. As expected, for both the geometrical arrangements, the reconstruction indexes improve when a greater number of illuminations is considered (Tab. II). In particular, γ_{int} reduces by about $\frac{1}{2}$ when V is extended from 4 to 8.

For comparison purposes, by considering the spherical arrangement with $V = 8$ illuminations, the reconstructions obtained with different methods using approximations have been analyzed. In more detail, the scattering process has been carried out using the first-order Born approximation [2], the second-order Born approximation, and the Rayleigh approximation [3]. Furthermore, the iterative Born method (BIM) [21] has been used as well as the "bare" (i.e., without the iterative multi-scaling process and the same level of spatial resolution in the overall investigation domain) CG-approach. The obtained results are reported in Tab. III in terms of computation time (T_k being the CPU-time needed for each iteration of the reconstruction process), discretization of the investigation domain (or RoI) N, total number of iterations K_{tot}, and reconstruction accuracy both qualitatively (ρ and Δ) and quantitatively (γ_{int}, γ_{ext}, and γ_{tot}). Whatever the approximation approach used, the localization error turns out to be two orders of magnitude greater than that of the IMSA-3D method. Similar conclusions hold for the error figure related to the extension of the scatterer domain Δ. The enhancement in the reconstruction accuracy can be also noticed concerning the quantitative indexes. However, such

an improvement causes an increase in the computational costs (i.e., the total number of iterations $K_{tot} = \sum_{s=1}^{S_{opt}} k_{conv}^{(s)}$, $k_{conv}^{(s)}$ being the number of iterations needed to achieve the "convergence" at the sth step of the multi-scaling process) even though, as expected, such an overhead turns out to be significantly smaller than that of the "bare" CG approach ($\frac{T_k\rfloor_{CG}}{T_k\rfloor_{IMSA-CG}} \cong 22$).

Finally, a structure more complex in shape has been considered to further validate the proposed approach. The unknown scatterer is an off-centered ($x_C = y_C = z_C = -0.075\,\lambda$) cross-shaped dielectric object ($\tau = 3.0$). Considering an arrangement similar to the previous experiment in terms of noisy conditions ($SNR = 20\,dB$), the reconstructed profile turns out to be accurate as indicated by the volume slices at $z = -0.075\,\lambda$ [Fig. $8(a)$] and $x = -0.075\,\lambda$ [Fig. $8(b)$] and confirmed by the values of the error figures ($\rho = 1.32 \times 10^{-3}$, $\Delta = 1.28 \times 10^{-1}$, $\gamma_{int} = 21.53$, $\gamma_{ext} = 0.58$, and $\gamma_{tot} = 0.79$).

5 Conclusions

An iterative multi-scaling strategy, based on an integral-equation formalism, has been presented for the solution of a full-vectorial three-dimensional inverse scattering problem. The approach considers an iterative multi-resolution process to fully exploit the available *a-priori* knowledge and to obtain a good trade-off between the computational complexity and the achievable spatial-resolution.

Reported numerical results, although preliminary, seem to indicate the feasibility of the proposed approach and the possibility of a qualitative as well as quantitative microwave imaging of three-dimensional dielectric profiles. Of course, due to the complexity of the full-vectorial 3D inverse scattering problem, several crucial points should be still addressed and solved. In such a framework, this paper constitutes only a first attempt to be further investigated. Towards this end, future works will be aimed at improving the method efficiency in terms of solution-space sampling as well as resolution accuracy by integrating more appropriate optimization algorithms. In particular, a computer code

based on a customized particle swarm optimizer (PSO) is currently under test. Moreover, it will be very important to obtain experimental data to verify the robustness of the proposed approach.

Acknowledgements

A. Massa wishes to thank E. Vico and C. Pedrazzani for their support. Moreover, the authors would express their gratitude to Dr. M. Donelli and A. Rosani for useful suggestions and discussions.

References

[1] Special Issue on "Microwave imaging and inverse scattering techniques," *J. Electromagn. Waves Applicat.*, vol. 17, Apr. 2003.

[2] S. Caorsi, S. Ciaramella, G. L. Gragnani, and M. Pastorino, "Microwave imaging by three-dimensional Born linearization to electromagnetic scattering," *Radio Sci.*, vol. 25, pp. 1221-1229, 1990.

[3] S. Caorsi, G. L. Gragnani, and M. Pastorino, "Three-dimensional inverse-scattering numerical solution within the Rayleigh approximation: preliminary results," *Microwave Opt. Technol. Lett.*, vol. 15, pp. 173-176, Jun. 1997.

[4] Y. Yu, T. Yu, and L. Carin, "Three-dimensional inverse scattering of a dielectric target embedded in a lossy half-space," *IEEE Trans. Geosci. Remote Sensing*, vol. 42, pp. 957-973, May 2004.

[5] H. Harada, M. Tanaka, and T. Takenaka, "Image reconstruction of a three-dimensional dielectric object using a gradient-based optimization," *Microwave Opt. Technol. Lett.*, vol. 5, pp. 332-336, Jun. 2001.

[6] A. Abubakar and P. M. van den Berg, "Three-dimensional inverse scattering applied to cross-well induction sensors," *IEEE Trans. Geosci. Remote Sensing*, vol. 38, pp. 1669-1681, Jul. 2000.

[7] Z. Q. Zhang and Q. H. Liu, "Three-dimensional nonlinear image reconstruction for microwave biomedical imaging," *IEEE Trans. Biomed. Eng.*, vol. 51, pp. 544-548, Mar. 2004.

[8] S. Caorsi, M. Donelli, D. Franceschini, and A. Massa, "A new methodology based on an iterative multiscaling for microwave imaging," *IEEE Trans. Microwave Theory Tech.*, vol. 51, pp. 1162-1173, Apr. 2003.

[9] S. Caorsi, G. L. Gragnani, and M. Pastorino, "A multiview microwave imaging system for two- dimensional penetrable objects," *IEEE Trans. Microwave Theory Tech.*, vol. 39, pp. 845-851, May 1991.

[10] J. Van Bladel, "Some remarks on Green's dyadic for infinite space," *IRE Trans. Antennas Propagat.*, vol. 9, pp. 563-566, Nov. 1961.

[11] R. F. Harrington, *Field Computation by Moment Method.* New York: McMillan, 1968.

[12] D. E. Livesay and K.-M. Chen, "Electromagnetic fields induced inside arbitrarily shaped biological bodies," *IEEE Trans. Microwave Theory Techn.*, vol. 22, pp. 1273-1280, Dec. 1974.

[13] O. M. Bucci, L. Crocco, T. Isernia, and V. Pascazio, "Subsurface inverse scattering problems: Quantifying qualifying and achieving the available information," *IEEE Trans. Geosci. Remote Sensing*, vol. 39, pp. 2527-2537, Nov. 2001.

[14] E. L. Miller and A. Willsky, "A multiscale, statistically based inversion scheme for linearized inverse scattering problems," *IEEE Trans. Geosci. Remote Sensing*, vol. 34, pp. 346-357, Mar. 1996.

[15] E. L. Miller, "Statistically based methods for anomaly characterization in images from observations of scattered fields," *IEEE Trans. Image Processing*, vol. 8, pp. 92-101, Jan. 1999.

[16] S. Caorsi, M. Donelli, and A. Massa, "Detection, location, and imaging of multiple scatterers by means of the iterative multiscaling method," *IEEE Trans. Microwave Theory Tech.*, vol. 52, pp. 1217-1228, Apr. 2004.

[17] A. Abubakar, P. M. van den Berg, and J. Mallorqui, "Imaging of biomedical data using a multiplicative regularized constrast source inversion method," *IEEE Trans. Microwave Theory Techn.*, vol. 50, pp. 1761-1771, Jul. 2002.

[18] R. V. Kohn and A. McKenney, "Numerical implementation of a variational method for electrical impedance tomography," *Inverse Problems*, vol. 6, pp. 389-414, Jun. 1990.

[19] T. Isernia, V. Pascazio, and R. Pierri, "On the local minima in a tomographic imaging technique," *IEEE Trans. Geosci. Remote Sensing*, vol. 39, pp. 1596-1607, Jul. 2001.

[20] M. Donelli and A. Massa, "A computational approach based on a particle swarm optimizer for microwave imaging of two-dimensional dielectric scatterers," submitted to *IEEE Trans. Microwave Theory Techn.*

[21] W. C. Chew, *Waves and Fields in Inhomogeneous Media*. New York: IEEE Press, 1995.

Figure Captions

- **Figure 1.** Schematic of the three-dimensional geometry. Multi-illumination/multi-view arrangement.

- **Figure 2.** Reconstruction of a centered cube ($x_C = y_C = z_C = 0.0$, $\ell = 0.3\,\lambda$, $\tau = 3.0$) - $SNR = 30\,dB$. Volume slices of the reconstructed dielectric distributions: (a) plane $z = 0.0$ and (b) plane $x = 0.0$[(2)].

- **Figure 3.** Reconstruction of a centered cube ($x_C = y_C = z_C = 0.0$, $\ell = 0.3\,\lambda$, $\tau = 3.0$). Behavior of the optimal value of the cost function during the optimization process.

- **Figure 4.** Reconstruction of a cube ($\ell = 0.3\,\lambda$, $\tau = 3.0$). Dependence of the error figures on the SNRs: (a) ρ, (b) Δ, (c) γ_{tot}, γ_{ext}, and γ_{int} (centered cube - continuous line ——— ; off-centered cube - dashed line ----------).

- **Figure 5.** Reconstruction of an off-centered cube ($x_C = y_C = z_C = 0.15\,\lambda$, $\ell = 0.3\,\lambda$, $\tau = 3.0$) - $SNR = 30\,dB$. Evolution of the 3D contours the reconstructed profiles at successive steps of the iterative multi-scaling procedure.

- **Figure 6.** Reconstruction of an off-centered cube ($x_C = y_C = z_C = 0.15\,\lambda$, $\tau = 3.0$) - $SNR = 20\,dB$. Dependence of the error figures on the object dimensions ($\frac{\ell}{\lambda}$): (a) qualitative error figures and (b) quantitative error figures.

- **Figure 7.** Reconstruction of an off-centered cube ($x_C = y_C = z_C = 0.15\,\lambda$, $\ell = 0.3\,\lambda$) - $SNR = 20\,dB$. Dependence of the error figures on the object function (τ): (a) qualitative error figures and (b) quantitative error figures.

- **Figure 8.** Reconstruction of an off-centered cross-shaped scatterer ($x_C = y_C = z_C = -0.075\,\lambda$ and $\tau = 3.0$) - $SNR = 20\,dB$. Volume slices of the reconstructed dielectric distributions: (a) plane $z = -0.075\,\lambda$ and (b) plane $x = -0.075\,\lambda$.

---

(2) Please note that the dashed line indicates the region occupied by the actual scatterer.

Table Captions

- **Table I.** Reconstruction of a centered cube ($x_C = y_C = z_C = 0.0$, $\ell = 0.3\,\lambda$, $\tau = 3.0$) - $SNR = 30\,dB$. Error figures.

- **Table II.** Reconstruction of an off-centered cube ($x_C = y_C = z_C = 0.15\,\lambda$, $\ell = 0.3\,\lambda$, $\tau = 3.0$) - $SNR = 20\,dB$. Error figures for different illumination conditions.

- **Table III.** Reconstruction of an off-centered cube ($x_C = y_C = z_C = 0.15\,\lambda$, $\ell = 0.3\,\lambda$, $\tau = 3.0$) - $SNR = 20\,dB$. Comparative assessment: error figures and computational costs.

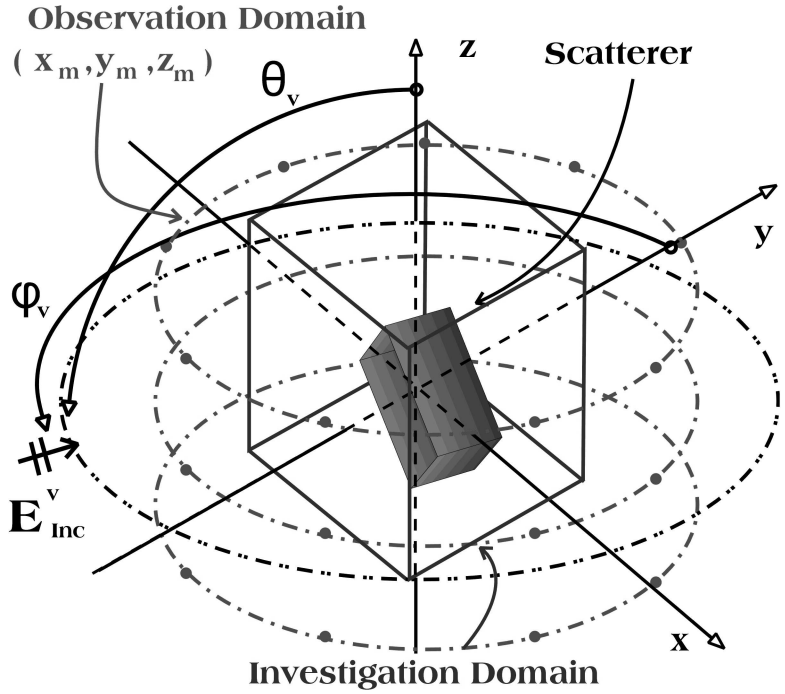

Fig. 1 - G. Franceschini *et al.*, "Full-vectorial three-dimensional microwave ..."

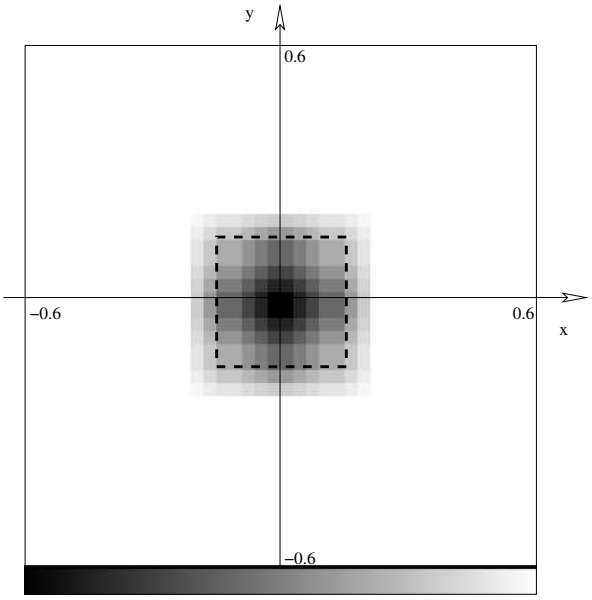

3.2 $Re\{\tau\,(x, y, z = 0.0)\}$ 0.0

(a)

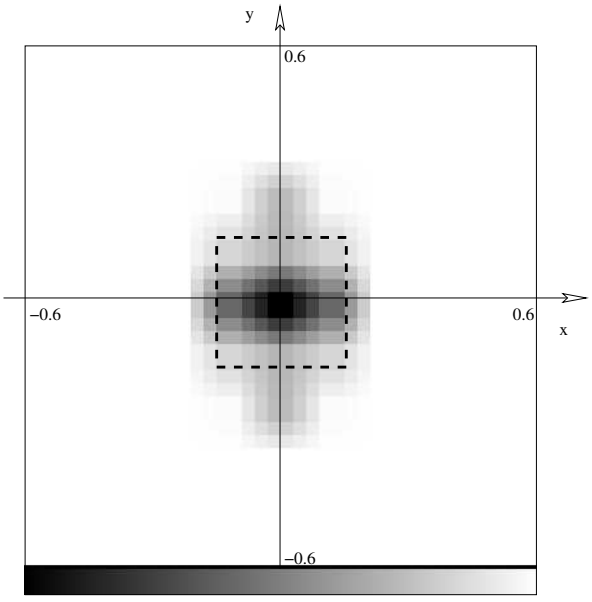

3.2 $Re\{\tau\,(x = 0.0, y, z)\}$ 0.0

(b)

Fig. 2 - G. Franceschini *et al.*, "Full-vectorial three-dimensional microwave ..."

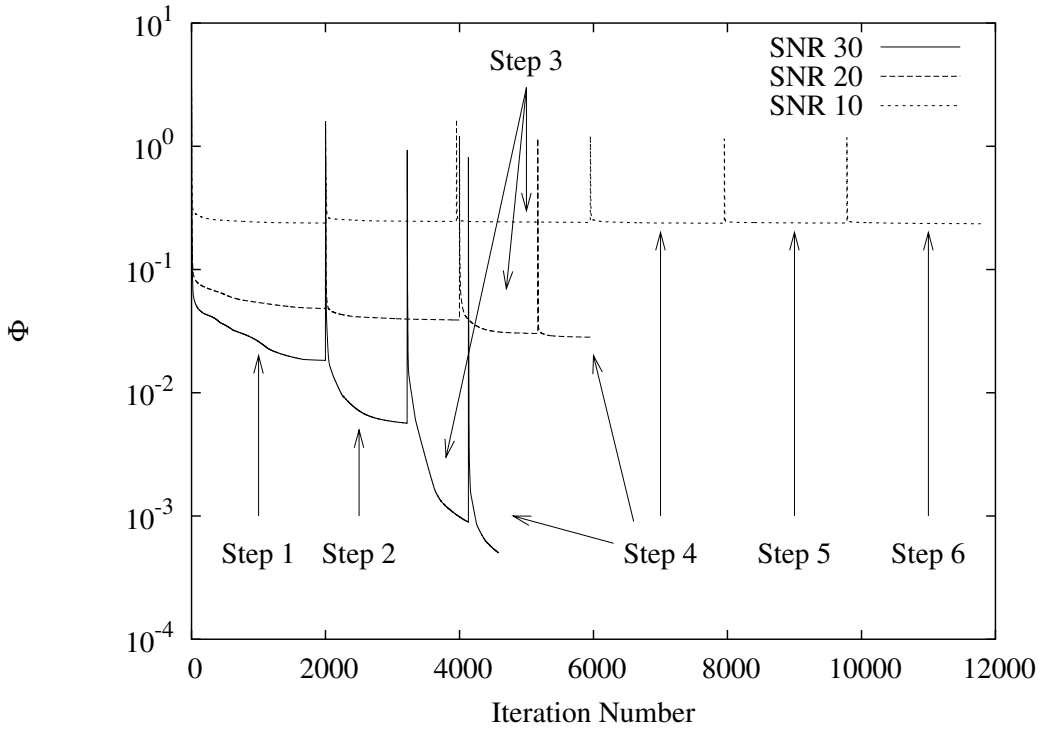

Fig. 3 - G. Franceschini *et al.*, "Full-vectorial three-dimensional microwave ..."

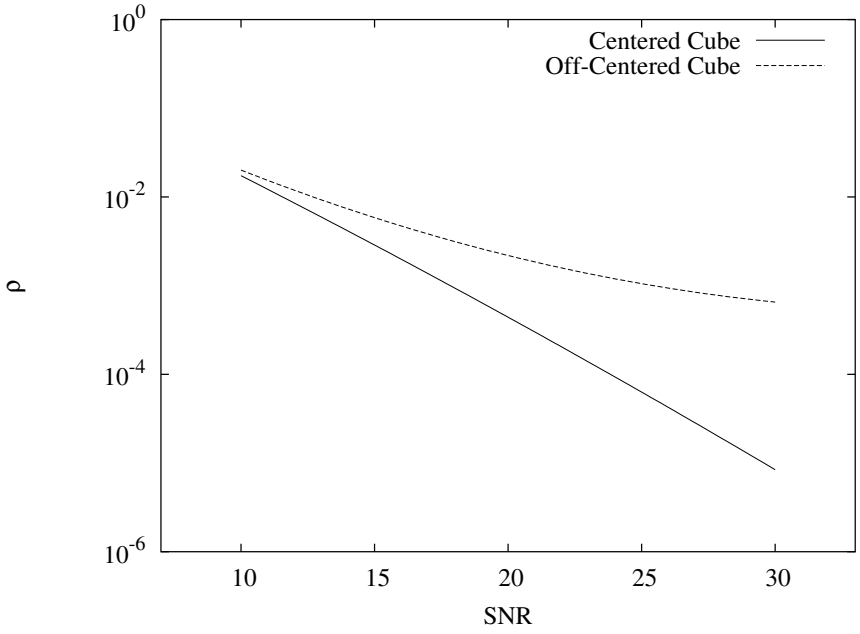

(a)

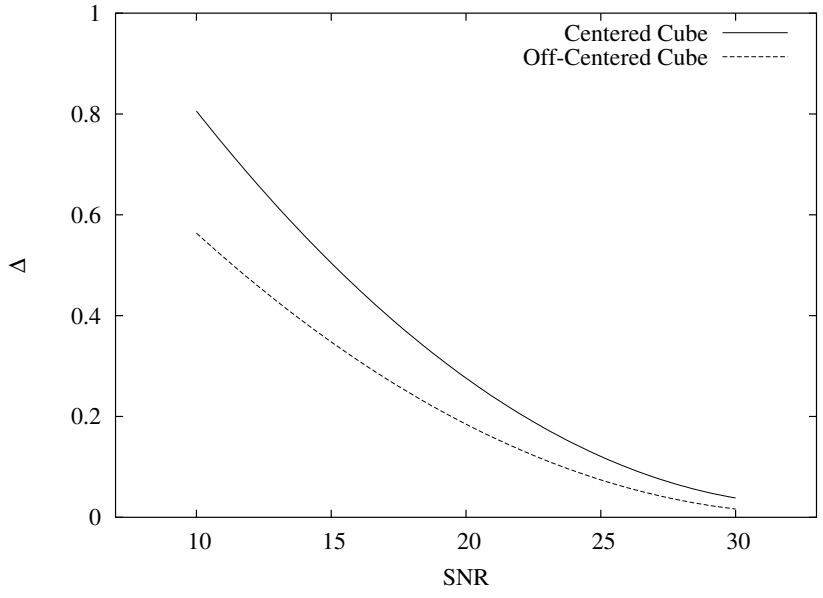

(b)

Fig. 4(I) - G. Franceschini *et al.*, "Full-vectorial three-dimensional microwave ..."

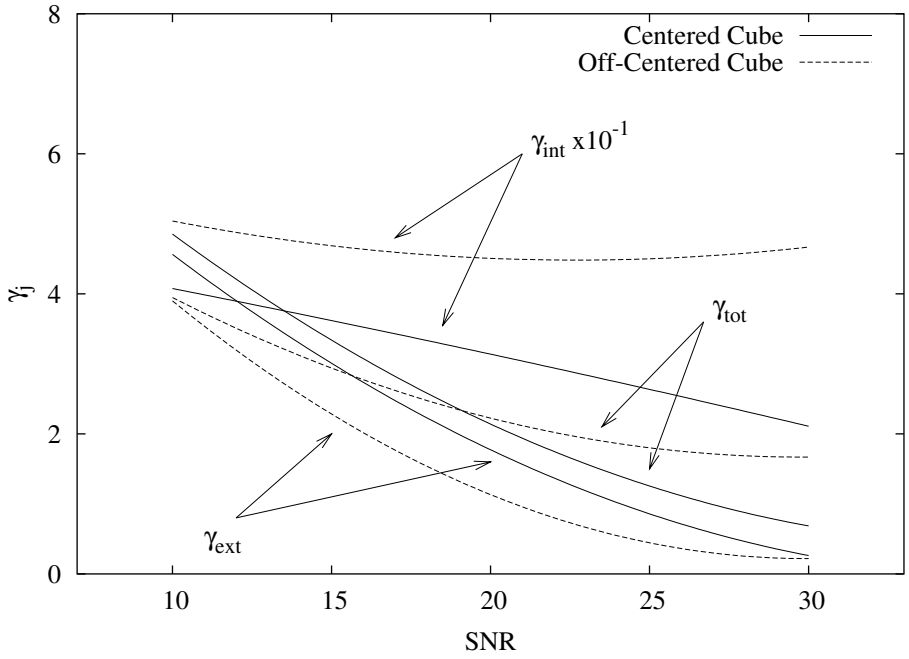

(c)

Fig. 4(*II*) - G. Franceschini *et al.*, "Full-vectorial three-dimensional microwave ..."

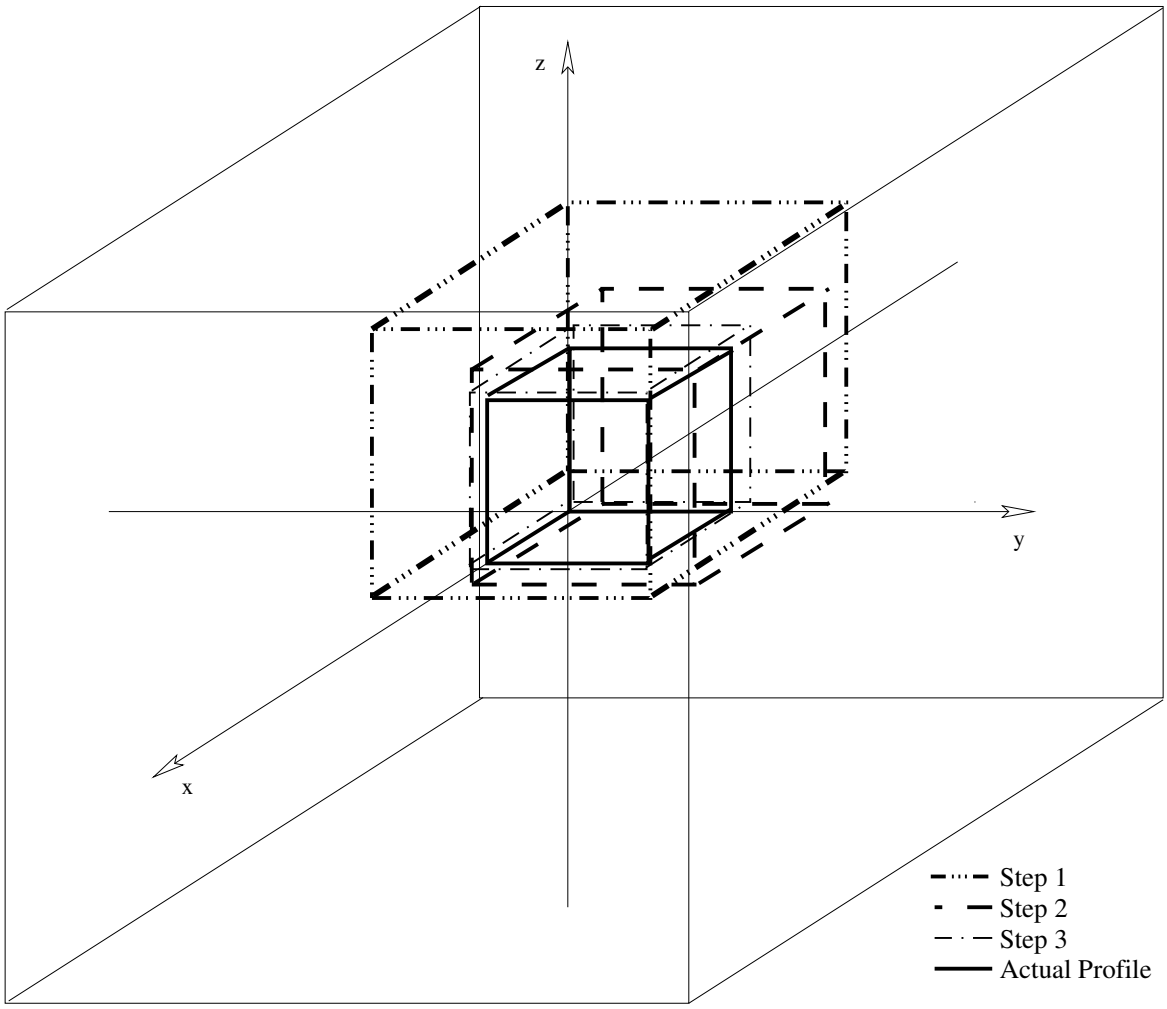

Fig. 5 - G. Franceschini *et al.*, "Full-vectorial three-dimensional microwave ..."

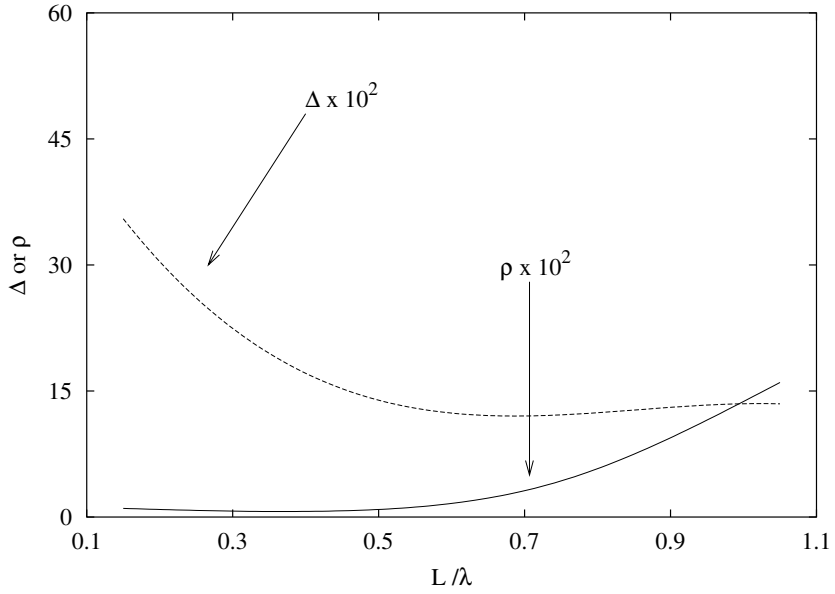

(*a*)

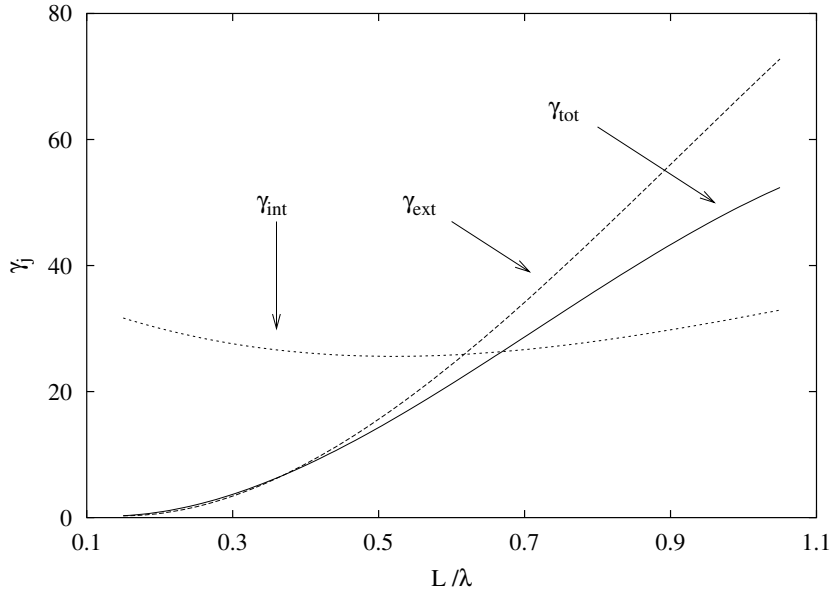

(*b*)

Fig. 6 - G. Franceschini *et al.*, "Full-vectorial three-dimensional microwave ..."

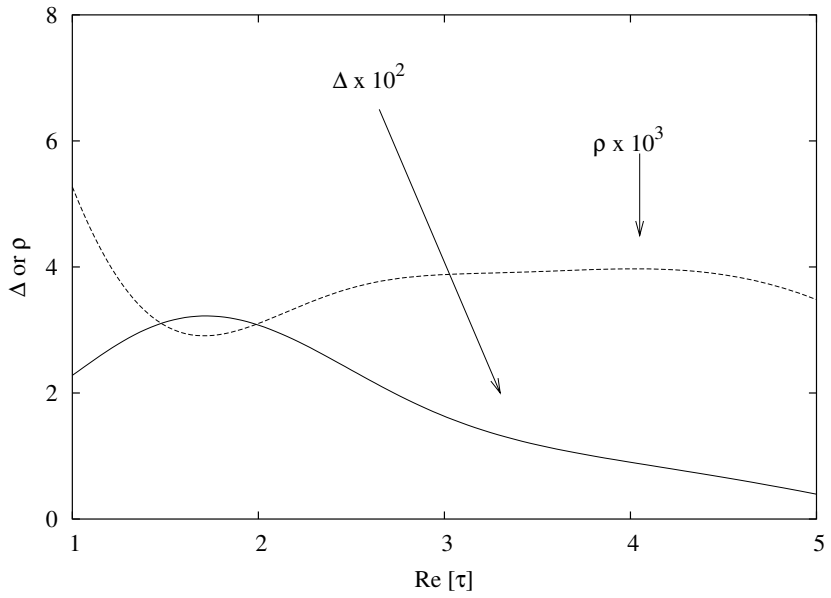

(a)

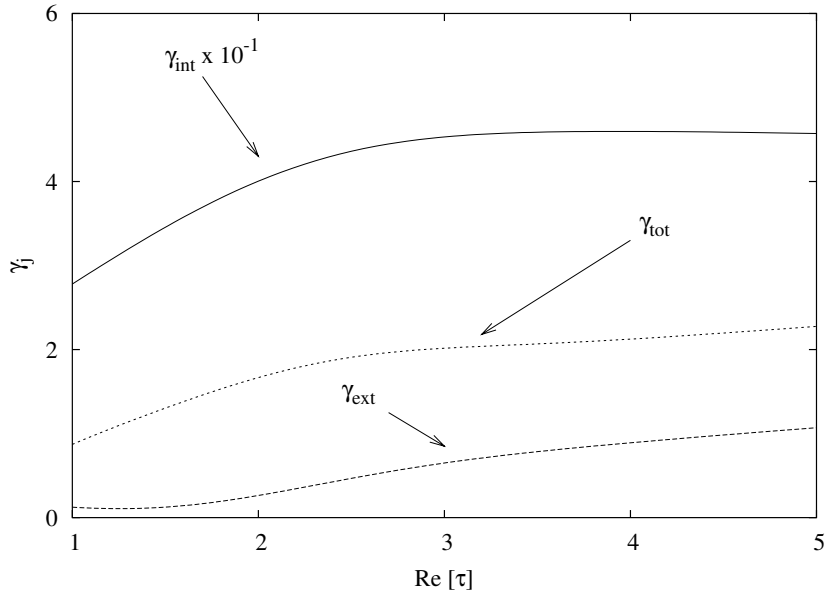

(b)

Fig. 7 - G. Franceschini *et al.*, "Full-vectorial three-dimensional microwave ..."

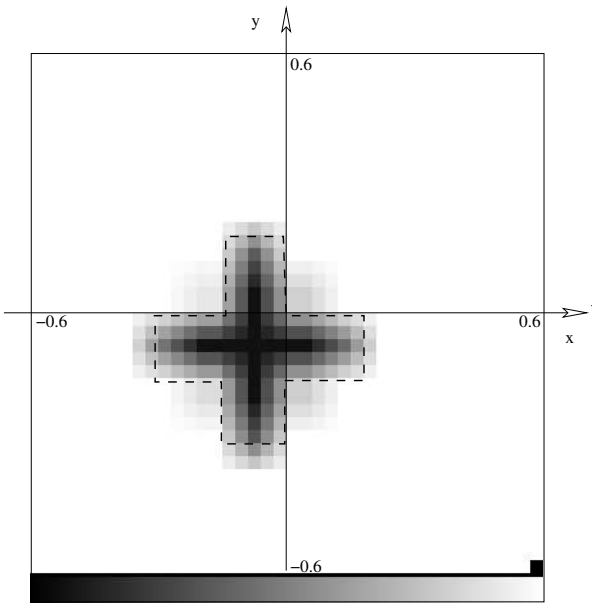

3.2 $Re\left\{\tau\left(x,\, y,\, \frac{z}{\lambda} = -0.075\right)\right\}$ 0.0

(a)

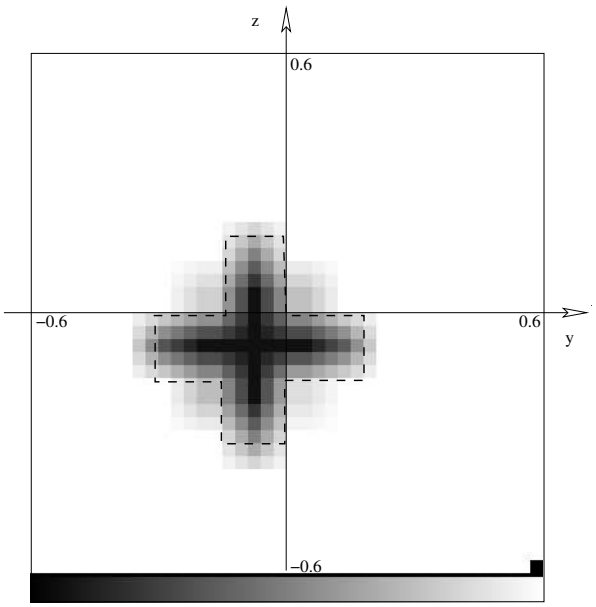

3.2 $Re\left\{\tau\left(\frac{x}{\lambda} = -0.075,\, y,\, z\right)\right\}$ 0.0

(b)

Fig. 8 - G. Franceschini *et al.*, "Full-vectorial three-dimensional microwave ..."

Step No.	γ_{tot}	γ_{ext}	γ_{int}	ρ	Δ
1	2.30	2.04	34.42	1.74×10^{-2}	2.35×10^{-1}
2	1.45	1.29	22.46	5.08×10^{-4}	9.32×10^{-2}
3	0.69	0.26	21.09	8.41×10^{-6}	3.83×10^{-2}

Tab. I - G. Franceschini *et al.*, "Full-vectorial three-dimensional microwave ..."

	Cylindrical			*Spherical*		
V	4	6	8	4	6	8
ρ	1.32×10^{-3}	6.41×10^{-3}	2.73×10^{-3}	3.8×10^{-3}	2.30×10^{-3}	7.99×10^{-4}
Δ	3.43×10^{-2}	2.21×10^{-2}	6.12×10^{-3}	1.94×10^{-2}	2.61×10^{-2}	2.81×10^{-2}
γ_{tot}	1.64	1.43	1.25	1.73	1.27	1.22
γ_{int}	41.60	29.48	28.60	44.37	33.44	28.11
γ_{ext}	0.11	1.08	0.82	0.08	0.33	0.94

Tab. II - G. Franceschini *et al.*, "Full-vectorial three-dimensional microwave ..."

	ρ	Δ	γ_{tot}	γ_{int}	γ_{ext}	N	K_{tot}	T_k $[sec]$
$Born\ I$	1.33×10^{-1}	1.26	3.90	62.17	2.29	10^3	1	3.74
$Born\ II$	1.52×10^{-1}	1.43	5.16	61.50	3.60	10^3	1	3.14
$Rayleigh$	1.41×10^{-1}	1.24	3.82	61.94	2.21	10^3	1	4.55
BIM	2.30×10^{-1}	1.66	9.83	61.75	8.39	10^3	200	3.10
CG	3.03×10^{-2}	3.89×10^{-1}	1.60	36.15	0.65	10^3	2000	70
$IMSA - CG$	7.99×10^{-4}	2.81×10^{-2}	1.27	28.11	0.94	5^3	4407	3.12

Tab. III - G. Franceschini *et al.*, "Full-vectorial three-dimensional microwave ..."